AIAA JOURNAL
Vol. 48, No. 7, July 2010

# Independent Two-Fields Solution for Full-Potential Unsteady Transonic Flows

A. Parrinello* and P. Mantegazza†
*Politecnico di Milano, 20156 Milano, Italy*

DOI: 10.2514/1.J050013

**The paper introduces a new approach for the numerical solution of full-potential unsteady flows based on an independent approximation of the density and velocity potential fields. The solution procedure relies on an unstructured, node-based, finite volume approximation, with linear shape functions and nonreflecting farfield boundary conditions. An improved upwind density biasing allows us to stabilize the solution in supersonic regions. In view of linearized aeroelastic stability and response analyses, unsteady boundary conditions are accounted for by means of a density flow transpiration. Time marching solutions are dealt using first/second-order implicit schemes, whose unconditional linearized stability properties are demonstrated. A few applications are presented to validate the method.**

## Nomenclature

| | | |
|---|---|---|
| $c$ | = | speed of sound, m/s |
| $C_L$ | = | lift coefficient |
| $C_M$ | = | moment coefficient |
| $C_p$ | = | pressure coefficient |
| $c_p$ | = | specific heat at constant pressure, J/kg/K |
| $c_v$ | = | specific heat at constant volume, J/kg/K |
| $H$ | = | total enthalpy, $m^2/s^2$ |
| $h$ | = | plunge motion |
| $H_{\text{am}}$ | = | aerodynamic transfer functions matrix |
| $k$ | = | reduced frequency |
| $M$ | = | Mach number |
| $V$ | = | velocity vector, m/s |
| $V^*$ | = | critical velocity, m/s |
| $\alpha$ | = | angle of attack, deg |
| $\gamma$ | = | heat capacity ratio |
| $\Delta$ | = | increment |
| $\theta$ | = | pitch motion, deg |
| $\rho$ | = | density, $Kg/m^3$ |
| $\phi$ | = | velocity potential, $m^2/s$ |
| $\varphi$ | = | reduced velocity potential: $\phi/V_\infty$, M |
| $*_t$ | = | time derivative of $*$ |
| $*_\infty$ | = | asymptotic value of $*$ |
| $\nabla\cdot$ | = | divergence operator |
| $\nabla$ | = | gradient operator |

## I. Introduction

INTEREST in nonlinear potential flow analyses for the investigation of realistic transonic problems surged in the early 1970s. Initially, the solution of the transonic small disturbance (TSD) equation was addressed. Along that line, one of the first viable solution schemes was developed by Murman and Cole [1] in 1971. They made an important observation concerning sub/supersonic domains by acknowledging the need of using centered differences within subsonic regions and backward differences within supersonic regions.

After Murman and Cole original paper, other researchers presented numerical methods for the solution of transonic flows. Steger and Lomax [2] introduced a solution based on relaxation with successive overrelaxations. Garabedian and Korn [3] developed a second-order accurate version of Murman and Cole scheme based on the full-potential (FP) equation in nonconservative form. Ballhaus and Bailey [4] and Bailey and Steger [5] solved transonic flows of real wings using the TSD equation.

In 1974, Jameson [6] devised a more flexible approach better caring of the local flow direction, the so called Jameson's rotated difference scheme.

Then Murman [7] showed that the potential equation had to be solved in conservation form to correctly satisfy jump conditions. In fact Murman solved the TSD equation using a nonconservative form but introduced a shock-point differencing operator. A year later Jameson [8] solved the FP equation in full conservation form, applying an artificial viscosity to the difference scheme used for supersonic regions.

Work using the finite element method took place during the 1970s too, albeit at a slightly slower pace. Few of the first transonic flow computations based on finite elements appeared in 1976 by Glowinsky et al. [9] and Ecer and Akay [10]. The first structured finite volume calculations followed by Jameson and Caughey [11] in 1977.

A different solution technique for the FP equation was presented in 1978 by Hafez et al. [12]. The conservative form of the FP equation was solved using artificial compressibility, whereas density was modified in regions of supersonic flow to provide an appropriate upwinding. This scheme was called density biasing.

In 1979 Jameson [13] gained further efficiency by applying a multigrid technique to the conservative FP equation. The increase in efficiency was confirmed by Boerstoel [14], who remarked that the shock position was not efficiently updated by the multigrid method. Different multigrid strategies and smoothing operators were extensively discussed by Van der Wees et al. [15].

The artificial compressibility technique was widely used by the early 1980s, when a new upwinding concept was introduced, called flux biasing or flux upwinding. Flux biasing helped capturing shock locations more accurately and eliminated most of the oscillations occurring around the related discontinuities. The idea was initially developed in 1980 by Engquist and Osher [16]. Early applications to the FP equation were presented by Boerstoel [14] (1982) and Osher [17] (1982). Flux biasing and density biasing schemes were compared by Volpe and Jameson [18].

In 1995 Holst [19] developed an FP flow solver using the Chimera approach. The algorithm can be applied to the three-dimensional flow over wings or wing/body geometries. An inner grid is used to describe the wing/body surface, while an outer grid describes the farfield region. The grids can overlap, taking advantage of the flexibility of Chimera grids.

Received 18 June 2009; revision received 08 January 2010; accepted for publication 09 February 2010. 

*Ph.D. Candidate, Dipartimento Ingegneria Aerospaziale, Via La Masa 34.
†Full Professor, Dipartimento Ingegneria Aerospaziale, Via La Masa 34.

In 1997 R. E. Neel [20] claimed the first unstructured finite volume FP solver for cell-centered meshes.

Through the 1990s and 2000s, research and development on potential flow lost appeal in favor of Euler and Navier–Stokes solvers, the speed and memory capability of new computers making their use affordable more and more.

Nonetheless, significant interest in FP solvers persists, the short computational time required by FP solutions makes them appealing to aircraft conceptual and preliminary design phases and for linearized aeroelastic analyses. So, even though FP solutions cannot be as accurate as Euler ones, the quintessence of the physics of an inviscid flow is captured. Furthermore, FP solutions can be used to initialize Euler/Navier–Stokes flow solvers, significantly reducing the iterations required for convergence.

The FP model loses validity in presence of shock discontinuities, where Rankine–Hugoniot relations [21] show a rise in entropy across the shock. Irrotationality is preserved only across uniform shocks. In many problems, the shock is curved. Therefore, entropy varies and the flow becomes rotational after the shock. Weak FP formulations allow a shock discontinuity to appropriately occur for mass and energy, but the shock remains isentropic and the momentum balance is not satisfied.

Nonetheless the entropy jump through a shock can be shown to be proportional to the third power of its intensity [21], $I$:

$$\Delta s = \frac{c_p}{12\gamma^3}(\gamma+1)(\gamma-1)I^3 + \mathcal{O}(I^4) \tag{1}$$

where $I = p_2/p_1 - 1$.

Thus the entropy production is relatively negligible for weak shocks, so a potential model represents an acceptable and effective approximation.

The present work introduces a new unstructured finite volume FP method. Its novelty is represented by the adoption of independent approximations for the density and potential fields that satisfy mass conservation and Bernoulli equation. The nonlinear ordinary differential equations in time resulting from the unstructured finite volume space discretization are solved through an implicit time integration. Unsteady solutions are mainly aimed at linearized transonic flutter calculations. So a transpiration formulation at the body boundary allows us to deal with unsteady cases typical of this class of problems, while using fixed meshes. The use of nonreflecting farfield boundary conditions allows relatively limited calculation domains. A modified upwind technique is used to better establish the right subsupersonic dependence based on geometrical considerations related to the local Mach cone. The resulting linearized implicit scheme is unconditionally stable for solutions with shocks.

The problem is formulated for subsonic asymptotic conditions, but the generality of the method allows its extension to supersonic asymptotic flows as well.

The following sections detail the new approach and its numerical implementation. Numerical results are also presented.

## II. Full Nonlinear Unsteady Potential Flow Model

The motion of an inviscid, isentropic and irrotational flow is defined by two scalar equations [21]: mass conservation,

$$\rho_t + \nabla\cdot(\rho\nabla\phi) = 0 \tag{2}$$

and Bernoulli equation,

$$\phi_t + \frac{|\nabla\phi|^2}{2} - \frac{V_\infty^2}{2} + \frac{c_\infty^2}{\gamma-1}\left(\left(\frac{\rho}{\rho_\infty}\right)^{\gamma-1} - 1\right) = 0 \tag{3}$$

The potential assumption involves irrotational flow. As a consequence the local vorticity production is zero, but there is a finite circulation around lifting bodies.

Denoting with $\Gamma_\infty(t)$ the circulation at a farfield contour around a two-dimensional airfoil and assuming that the airfoil starts moving from rest, using Kelvin's theorem, we have: $\Gamma_\infty(t) = \Gamma_\infty(0) = 0$.

Then, due to the multiply connected domain, a nonuniqueness arises from the wake, a zero-thickness vortex layer, which is a line of discontinuity for the potential function [22]. The fact that the circulation $\Gamma_\infty(t)$ over a suitably large contour vanishes implies that $\Gamma_B(t) = -\Gamma_W(t)$, where $\Gamma_B$ denotes the circulation around the body and $\Gamma_W$ the circulation around the wake.

A similar situation occurs for three-dimensional steady and unsteady flows around isolated wings. In this case the domain is simply-connected, the potential is single-valued and the wake is a surface of discontinuity for the potential function.

In order to freely satisfy mass conservation across the potential discontinuity, pressure continuity between the lower ($l$) and upper ($u$) side of this line|surface is imposed. So Eq. (3) allows us to write

$$(2\phi_t + |\nabla\phi|^2)_l = (2\phi_t + |\nabla\phi|^2)_u \tag{4}$$

After defining the curvilinear coordinate $\xi$ on the wake and requiring the flow to be tangential to it, Eq. (4) becomes

$$\left(2\phi_t + \left(\frac{\partial\phi}{\partial\xi}\right)^2\right)_l = \left(2\phi_t + \left(\frac{\partial\phi}{\partial\xi}\right)^2\right)_u \tag{5}$$

Calling the potential jump through the wake $\Delta\phi(\xi,t) = \phi_l(\xi,t) - \phi_u(\xi,t)$, the convective equation

$$\frac{\partial(\Delta\phi)}{\partial t} + \bar{u}\cdot\nabla(\Delta\phi) = \frac{D(\Delta\phi)}{Dt} = 0 \tag{6}$$

is obtained, where $\bar{u}$ is the mean tangential velocity.

Finally the tangential flow condition needs to be applied on the body surface:

$$V^n_{\text{relative}} = V^n_{\text{flow}} - V^n_{\text{body}} = \frac{\partial\phi}{\partial n} - V^n_{\text{body}} = 0 \tag{7}$$

### A. Nonreflecting External Boundary Conditions

The unsteady potential equation is hyperbolic, so the number of physical variables that can be imposed on the external farfield boundary is related to the propagation properties of the system perturbations. For asymptotic subsonic flows we must impose only one condition on the farfield boundary, to prevent reflections.

The standard technique used to achieve such a condition is related to the characteristic variables [23] and leads to the imposition of the farfield normal inflow. The one-dimensional nonreflecting condition is [23]

$$u = u_\infty \pm \frac{\phi_t}{c_\infty \mp u_\infty} \tag{8}$$

For a multidimensional domain, Eq. (8) becomes

$$\frac{\partial\phi}{\partial n} = V^n_\infty \pm \frac{\phi_t}{c_\infty \mp V^n_\infty} \tag{9}$$

where $V^n_\infty$ is the normal component of the asymptotic speed on the boundary.

This technique leads to a nonreflecting condition that is exact for one-dimensional cases only, but remains an acceptable approximation for multidimensional cases when applied normally to the boundary.

### B. Scaled Equations

Equations are scaled with respect to the asymptotic values $\rho_\infty$ and $V_\infty$, leaving lengths dimensioned. So, denoting dimensional quantities with the suffix $d$, we define the following quantities:

$$\rho = \rho_d/\rho_\infty, \qquad \varphi = \phi_d/V_\infty, \qquad t = V_\infty t_d$$

Equations (2) and (3) become

$$\rho_t + \nabla(\rho\nabla\varphi) = 0 \tag{10}$$

$$\varphi_t + \frac{1}{2}(|\nabla\varphi|^2 - 1) + \frac{M_\infty^{-2}}{\gamma - 1}(\rho^{\gamma-1} - 1) = 0 \tag{11}$$

with

$$M = M_\infty |V| \rho^{\frac{1-\gamma}{2}}, \qquad C_p = 2(\rho^\gamma - 1)/(\gamma M_\infty^2), \qquad k = \omega / V_\infty$$

### C. Two-Fields Model

A Potential flow is based on mass and energy conservation, Eq. (10) and (11), with farfield boundary conditions given by Eq. (9), boundary conditions on the body given by Eq. (7) and wake conditions given by Eq. (6).

The most common strategy adopted so far to solve potential flows, e.g., see [24], is to evaluate the density using Bernoulli equation, Eq. (11):

$$\rho = \left[1 - \frac{\gamma - 1}{2} M_\infty^2 (2\varphi_t + |\nabla\varphi|^2 - 1)\right]^{\frac{1}{\gamma-1}} \tag{12}$$

substituting it in the mass conservation, Eq. (10). This results in a conservative second-order differential scheme in the unknown $\varphi$ only.

The novelty of the method adopted in this work consists of keeping Eqs. (10) and (11) and defining $\rho$ and $\varphi$ independently. With a mechanical analogy $\varphi$ can be identified as a degree of freedom function while the pair $\rho - \varphi$ can be interpreted as state functions. This corresponds to formulating the problem in state space form.

The two state fields model considerably simplifies the development of a numerical approximation, leading to a robust resolution scheme. One could object that this scheme loses the advantage of a single unknown field. This remark is only cursory true as, in view of the high sparsity of the resulting solution scheme, the substitution of Eq. (11) into Eq. (10) is tantamount to what is done by any sparse solver.

Moreover the mentioned simplification in setting up a numerical solution allows us to avoid the use of many bags of tricks that would be required by substituting Eq. (12) in an unstructured finite volume $\varphi$-only approach, e.g., in implementing: a tuned upwind scheme, an exact Jacobian for implicit integration schemes, the enforcement of the entropy jump across the shock in terms of $\rho$.

## III. Unstructured Finite Volume Numerical Solution

We will apply a node-based/centered finite volume discretization in space, leading to a set of first-order nonlinear ordinary differential equations in time. This finite volume approach can also be seen as a weighted residuals finite element scheme with piecewise constant weighting on each computational cell combined with an integration by part. Such a double face interpretation of finite volumes is trivial. It is nonetheless stressed because our presentation of per volume operations will be more akin to a finite element than a finite volume framework.

Regardless of the way they are derived, the related equations in weak form are: mass conservation,

$$\frac{\partial}{\partial t}\int_\Omega \rho \, \mathrm{d}\Omega + \oint_\Sigma \rho \nabla\varphi \cdot \mathbf{n} \, \mathrm{d}\Sigma = 0 \tag{13}$$

Bernoulli equation,

$$\frac{\partial}{\partial t}\int_\Omega \varphi \, \mathrm{d}\Omega + \int_\Omega \left[\frac{1}{2}(|\nabla\varphi|^2 - 1) + \frac{M_\infty^{-2}}{\gamma - 1}(\rho^{\gamma-1} - 1)\right] \mathrm{d}\Omega = 0 \tag{14}$$

The above weak balance Eqs. (13) and (14), combined with Eqs. (6), (7), and (9), account for discontinuous solutions also.

### A. Spatial Discretization

The spatial discretization uses triangles and tetrahedrons, i.e., the elements. Element vortices are indicated as nodes and the domain portions related to each node as cells, i.e., the finite volumes. The finite volume related to the $j$th node is highlighted by dashed lines at the left of Fig. 1. The solution variables are located on nodes and the approximation for both $\rho$ and $\varphi$ is based on linear shape functions within each element.

### B. Mesh and Elements Data Processing

The proposed formulation can be implemented in two ways. One consists of preparing cell fluxes on a per element basis, assembling nodal equations as in finite element method implementations. The other one indexes elemental data globally, placing them in global sparse matrices and obtaining the equations to be solved with a few simple general sparse matrix operations. For our initial proof of concept implementation the second approach has been used, because it is easier and simpler to implement. Its efficiency relies on suitable sparse matrix manipulation libraries. The related tools are available as free(dom) software.

The geometric treatment of the mesh concerns only its elements. A matrix containing the vortices coordinates of the $i$th element is defined:

$$M_N^i = \begin{bmatrix} x_1^i & y_1^i & \dots & 1 \\ x_2^i & y_2^i & \dots & 1 \\ \vdots & \vdots & & \vdots \\ x_{N+1}^i & y_{N+1}^i & \dots & 1 \end{bmatrix} \tag{15}$$

Where $N$ denotes the domain dimension (2 or 3). Then we calculate the domain portion related to each element:

$$\text{Area}\,|\text{volume}_i = |\det(M_N^i)|/N! \tag{16}$$

The matrix operators that allow to compute the gradient of the linear approximating shape functions are derived from these matrices. The global gradient operator is

$$\{\text{Grad}(f)_k\}_m = [G_k]_{m \cdot n}\{f\}_n \tag{17}$$

where vector $\{f\}$ collects the function values at the $n$ nodes and vector $\{\text{Grad}(f)_k\}$ collects the values of the $k$ component of the function gradient whitin the $m$ elements.

Figure 1 shows how elements are handled. The elements are divided by medians in a number of parts equal to the number of vortices. The portion of the $i$th element related to the $j$th node is highlighted on the left by dashed lines. The portion of domain related to each cell can be computed from the portion of domain related to each element:

$$\{\text{Area}|\text{volume}_{\text{cell}}\}_n = \{A\}_n = [\Sigma]_{n \cdot m}\{1\}_m \tag{18}$$

where $[\Sigma]$ is a sparse matrix that computes the integral on the cells of a constant function within each element. The element $(j, i)$ of $[\Sigma]$ is the portion of the $i$th element related to the $j$th cell. The nonnull elements of column $i$ are either equal to a third of the $i$th triangle area or to a quarter of the $i$th tetrahedron volume.

With the geometrical treatment shown at the left of Fig. 1, an exact estimation of the mass fluxes within the elements flux sub faces can be obtained. Moreover, the topological treatment of the elements and global equations assembly can be simplified by further approximating the calculation of internal fluxes. This approximation consists of calculating the fluxes by using only the density at the center of each element. The geometrical treatment shown at the right of Fig. 1 is obtained. The integrated normal components are collected in vectors $\{\hat{n}_k^h\}_m$ of dimension equal to the number of elements, where $k$ indicates the component and $h$ the element node number. Six and 12 vectors in two- and three-dimensional problem are obtained, respectively.

The density at the center of each element is computed as the average of the values at the vortices:

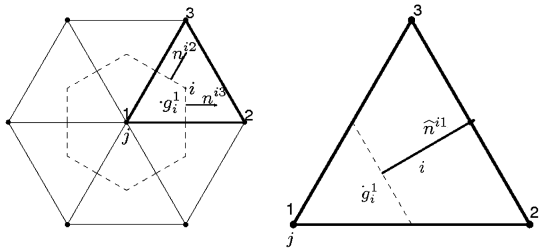


**Fig. 1 Two-dimensional element handling.**

$$\{\rho_g\}_m = [B_g]_{m\cdot n}\{\rho\}_n \tag{19}$$

where matrix $[B_g]_{m\cdot n}$ combines incidence and integration weights. The nodal fluxes are computed as

$$\{F_{\text{cell}}\}_n = \sum_h [B_h]_{n\cdot m} \sum_k \{V_k\}_m \{\rho_g\}_m \{\hat{n}_k^h\}_m \tag{20}$$

To assemble the final equations, the integration on the cells of a linear function within each element is required. This is performed by a quadrature of the function at the centers of the domain portions ($g_i^h$ in Fig. 1). Such an integration is exact for linear functions only. The function values at the quadrature points are related to the nodal values with

$$\begin{Bmatrix} \bar{\rho}_1 \\ \bar{\rho}_2 \\ \bar{\rho}_3 \end{Bmatrix}_i = \frac{1}{36}\begin{bmatrix} 22 & 7 & 7 \\ 7 & 22 & 7 \\ 7 & 7 & 22 \end{bmatrix}\begin{Bmatrix} \rho_1 \\ \rho_2 \\ \rho_3 \end{Bmatrix}_i$$

$$\begin{Bmatrix} \bar{\rho}_1 \\ \bar{\rho}_2 \\ \bar{\rho}_3 \\ \bar{\rho}_4 \end{Bmatrix}_i = \frac{1}{144}\begin{bmatrix} 75 & 23 & 23 & 23 \\ 23 & 75 & 23 & 23 \\ 23 & 23 & 75 & 23 \\ 23 & 23 & 23 & 75 \end{bmatrix}\begin{Bmatrix} \rho_1 \\ \rho_2 \\ \rho_3 \\ \rho_4 \end{Bmatrix}_i$$

for the $i$th triangle and tetrahedron, respectively. These matrices, and each element area/volume, allow to build the matrix integration operator:

$$\{\rho_{\text{int}}\}_n = [I]_{n\cdot n}\{\rho\}_n \tag{21}$$

The potential discontinuity at the wake adds as many unknown values of $\varphi$ as the wake nodes, so distinct integration matrices are needed for $\rho$ and $\varphi$.

### C. Treatment of Supersonic Regions

Transonic flow fields have subsonic and supersonic space regions. Subsonic regions are elliptic and each point within the related domain is influenced by every other point. As the flow becomes supersonic, the nature of the flow changes to hyperbolic and a domain of dependence is formed whereas the flow properties at a single point are affected by what is happening in an upstream domain only. In a similar way a domain of influence exists where a point in the flow can only impact other points that lie in a domain downstream of the point. When domains of dependence and influence exist, information in the subsonic field traveling upstream must move around the supersonic region. Sonic lines/surfaces and shock waves appear in these situations and provide boundaries between elliptic and hyperbolic regions.

The finite volume scheme implies a central discretization, so an upwind desymmetrization bias needs to be introduced to impose spatial causality in supersonic regions.

A standard technique is used for the treatment of supersonic regions. It consists of introducing an artificial viscosity [25] based on a modified density $\tilde{\rho}$ to achieve a correct domain dependence for the solution [21]:

$$\tilde{\rho} = \rho + \Delta\rho \tag{22}$$

where $\Delta\rho$ must provide a value of $\tilde{\rho}$ that corresponds to a value of $\rho$ internal to the upstream Mach cone. Then $\Delta\rho$ can be expressed as a variation of $\rho$ along the flow direction for a distance $-\Delta l$:

$$\Delta\rho = -\nabla\rho \cdot \frac{\nabla\varphi}{|\nabla\varphi|}\Delta l \tag{23}$$

where $\Delta l$ is unknown. The above flux biasing is used only for flux calculations in the cells, so the upwinding scheme must be applied to $\rho$ at the center of an element. The value of $\Delta l$ is then determined by considering a characteristic length $l_i$ for each element:

$$\Delta l_i \propto l_i \tag{24}$$

where $l_i = \sqrt{\text{Area}_i}$ for the $i$th triangle and $l_i = \sqrt[3]{\text{Volume}_i}$ for the $i$th tetrahedron.

Different techniques can be used to define the proportionality in Eq. (24). A standard density upwind scheme [23] is

$$\Delta l_i = l_i \cdot \varepsilon \tag{25}$$

whereas $\varepsilon$ is a unique proportionality constant defined for the whole supersonic domain. The supersonic region where the upwind must be applied needs to be determined. The velocity modulus is compared with the local critical velocity of each element:

$$|V_i| > V_i^* \rightarrow \Delta l_i = l_i \cdot \varepsilon \tag{26}$$

$$|V_i| < V_i^* \rightarrow \Delta l_i = 0 \tag{27}$$

The local critical velocity is

$$V_i^* = \sqrt{\frac{2 + (\gamma-1)M_\infty^2}{(\gamma+1)M_\infty^2}V_\infty^2 - 2\frac{\gamma-1}{\gamma+1}\dot{\varphi}_i} \tag{28}$$

The standard upwind scheme is widely used in the literature and provides good results. Nevertheless, it needs to be calibrated with respect to the supersonic condition.

The modified technique developed in the present work allows us to avoid any calibration. It takes into account the geometry of the Mach cones at the element vortices as shown at the right of Fig. 2. The proportionality between $\Delta l_i$ and the tangent of the angle $\alpha_i$ is imposed:

$$\Delta l_i \propto \tan(\alpha_i) = \sqrt{M_i^2 - 1} \tag{29}$$

This yields a relation for the whole domain depending on the local Mach number $M_i$:

$$\Delta l_i = l_i \cdot \varepsilon \cdot \text{Real}\,(\sqrt{M_i^2 - 1}) \tag{30}$$

so that $\varepsilon$ becomes the only free parameter. A suitable value of $\varepsilon$ is within the 0.8–0.9 range. This yields also a continuous upwind activation, as shown at the left of Fig. 2, which contributes to numerical stability.

The density variations within the $m$ elements, collected in the vector $\{\Delta\rho\}$, after applying Eq. (23), is

$$\{\Delta\rho\} = -\text{diag}\left\{\frac{\Delta l}{|V|}\right\}\sum_k (\text{diag}([G_k]\{\varphi\})[G_k])\{\rho\} = [U]\{\rho\} \tag{31}$$

The density $\rho$ at the center, needed to compute the fluxes of Eq. (20), becomes

$$\{\rho_g\} = ([B_g] + [U])\{\rho\} \tag{32}$$

### D. External Farfield Boundary Conditions

Recalling Eq. (9), a domain with an asymptotic flow in the $x$ direction is considered. Vector $\{n_x\}_{\text{ext}}$ collects the $x$ component of the integrated normals of the farfield surface at the external nodes and $\{|n|\}_{\text{ext}}$ collects the magnitudes of the integrated normals. The normal velocity at boundary nodes becomes

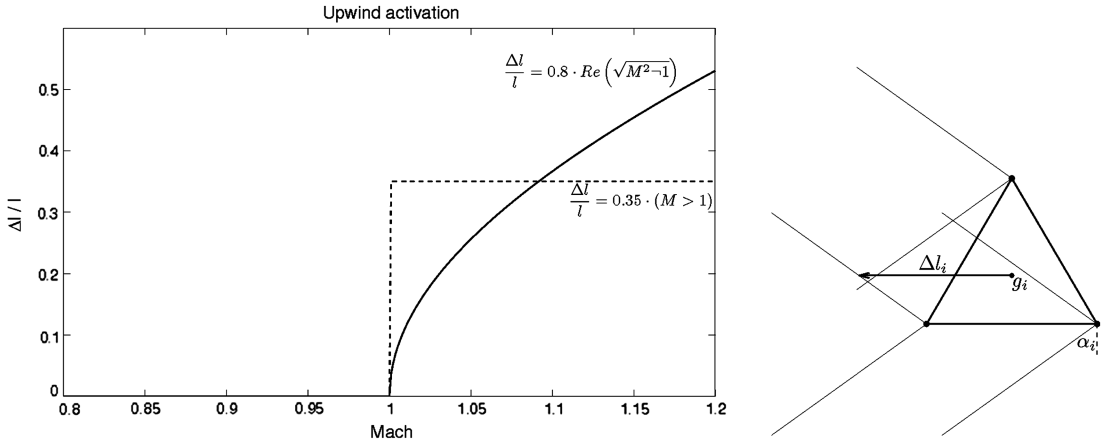


**Fig. 2 Upwind activation (left) and interpretation (right) for the proposed scheme.**

$$\left\{\frac{\partial\varphi}{\partial n}\right\}_{\text{ext}} = \frac{\{n_x\}_{\text{ext}}}{\{|n|\}_{\text{ext}}} + \text{diag}\left\{\frac{\partial\varphi}{\partial t}\right\}_{\text{ext}} \frac{\text{sign}(\{n_x\}_{\text{ext}})}{\{\frac{1}{M_\infty}\} - \frac{\{n_x\}_{\text{ext}}}{\{|n|\}_{\text{ext}}}} \tag{33}$$

where divisions must be considered as element-by-element divisions. A density flux appears at the boundary:

$$\{\Delta F\}_{\text{ext}} = \text{diag}\left\{\frac{\partial\varphi}{\partial n}\right\}_{\text{ext}} \text{diag}\{|n|\}_{\text{ext}}\{\rho\}_{\text{ext}} \tag{34}$$

### E. Boundary Conditions on the Body

A rigorous treatment of unsteady conditions needs a moving mesh. However, since our primary goal is to use a nonlinear potential flow to study transonic flutter, only small boundary motions are considered. This allows us to use transpiration: the mesh is locked and the body motion is simulated by assigning the corresponding normal speed to the boundary nodes. Then an incremented density flux appears at the boundary:

$$\{\Delta F\}_{\text{body}} = \text{diag}\{V_n\}_{\text{body}} \text{diag}\{|n|\}_{\text{body}}\{\rho\}_{\text{body}} \tag{35}$$

where the vector $\{V_n\}_{\text{body}}$ is related to body motions, and vector $\{|n|\}_{\text{body}}$ is analogous to vector $\{|n|\}_{\text{ext}}$.

### F. Wake Conditions

Figure 3 illustrates trailing edge and wake nodes. A unique value of $\rho$ and two values of $\varphi$ are assigned to each wake node, but only one control volume is defined for both $\rho$ and $\varphi$ equations.

The convective wake equation, Eq. (4), in discrete form becomes

$$\frac{\partial}{\partial t}(\{\varphi_{\text{up}}\}_{\text{wake}} - \{\varphi_{\text{low}}\}_{\text{wake}}) = -\frac{1}{2}(\{|V|^2_{\text{up}}\}_{\text{wake}} - \{|V|^2_{\text{low}}\}_{\text{wake}}) \tag{36}$$

Nevertheless, the velocity term is related to the elements, while the potential term is related to the nodes. Each wake node $i$ is related to one element for each wake side: $\text{up}_i$ and $\text{low}_i$. The elements $\text{up}_i$ and $\text{low}_i$ are the upstream elements related to node $i$ respectively above and below the wake.

The potential discontinuity adds as many unknown terms as the wake nodes, so Eq. (36) restores the balance between equations and unknowns.

It should be remarked that vectors $\{\rho\}$ and $\{\varphi\}$ have different dimensions, so some operators for $\rho$ are different from the same operators for $\varphi$. Calling $n$ the total number of nodes, $m$ the total number of elements, $w$ the number of wake nodes and defining $p = n + w$, we obtain

$$\{\rho_{/k}\}_m = [G_{\rho k}]_{m\cdot n}\{\rho\}_n, \qquad \{\varphi_{/k}\}_m = [G_{\varphi k}]_{m\cdot p}\{\varphi\}_p$$
$$\{\rho_{\text{int}}\}_n = [I_\rho]_{n\cdot n}\{\rho\}_n, \qquad \{\varphi_{\text{int}}\}_n = [I_\varphi]_{n\cdot p}\{\varphi\}_p$$

### G. Shock Conditions

Equations (13) and (14) can embed discontinuous solutions and the treatment of supersonic regions with Eq. (22) allows us to stabilize a shock in transonic conditions. However, because of the density continuity in the domain, the shock is not a real jump within an approximated solution, so a fine spatial discretization of its region is needed to correctly resolve a sharp shock. If the shock position is not known a priori, a local refinement technique may not be trivial. An alternative way to obtain a sharp shock consists of introducing a real discontinuity for the density function across the shock, by imposing the correct nonisentropic jump, given by the Rankine–Hugoniot relation [21]:

$$\frac{\rho_2}{\rho_1} = \frac{\phi_{n1}}{\phi_{n2}} = \frac{(\gamma+1)M^2_{n1}}{2 + (\gamma-1)M^2_{n1}} = f(M_{n1}) \tag{37}$$

where 1 and 2 denote the shock upstream and downstream, respectively, $n$ denotes the local shock normal and $M_{n1} = (V_{n1} - V_{\text{shock}})/c_1$.

The shock assumption ($H = \text{const}$) and Bernoulli theorem ($\phi_t + H = \text{const}$) imply the continuity of the potential across the shock. This does not prevent the proper normal velocity discontinuity related to Eq. (37). So the proposed two-fields scheme is very convenient for a natural shock description.

According to what outlined above an additional algebraic equation for each node of the shock is needed:

$$\{\rho_{\text{down}}\}_{\text{shock}} = \text{diag}\{f(M_n)\}_{\text{shock}}\{\rho_{\text{up}}\}_{\text{shock}} \tag{38}$$

In order to identify the shock nodes, the upstream and downstream Mach numbers are checked at each node.

As shown in the results section, a simple and efficient implementation consists of duplicating the values of $\rho$ only at the body nodes.

### H. Discrete Equations

Using the matrices presented in the previous paragraphs the discretized overall mass conservation, Eq. (13), is

$$[I_\rho]\left\{\frac{\partial\rho}{\partial t}\right\} = \{F\} \tag{39}$$

where matrix $[I_\rho]$ integrates the $\rho$ derivative on the cells from the nodal values, and vector $\{F\}$ collects the cells fluxes.

The discrete form of Bernoulli equation in weak form, Eq. (14), is

$$[I_\varphi]\left\{\frac{\partial\varphi}{\partial t}\right\} = -\frac{1}{2}[\Sigma](\{|\nabla\varphi|^2\} - \{1\}) - \frac{M^{-2}_\infty}{\gamma-1}[I_\rho](\{\rho^{\gamma-1}\} - \{1\}) \tag{40}$$

where matrix $[I_\varphi]$ integrates the derivative of $\varphi$ on the cells from the nodal values, and matrix $[\Sigma]$ integrates element constant functions on the cells, as defined in Sec. III.B.

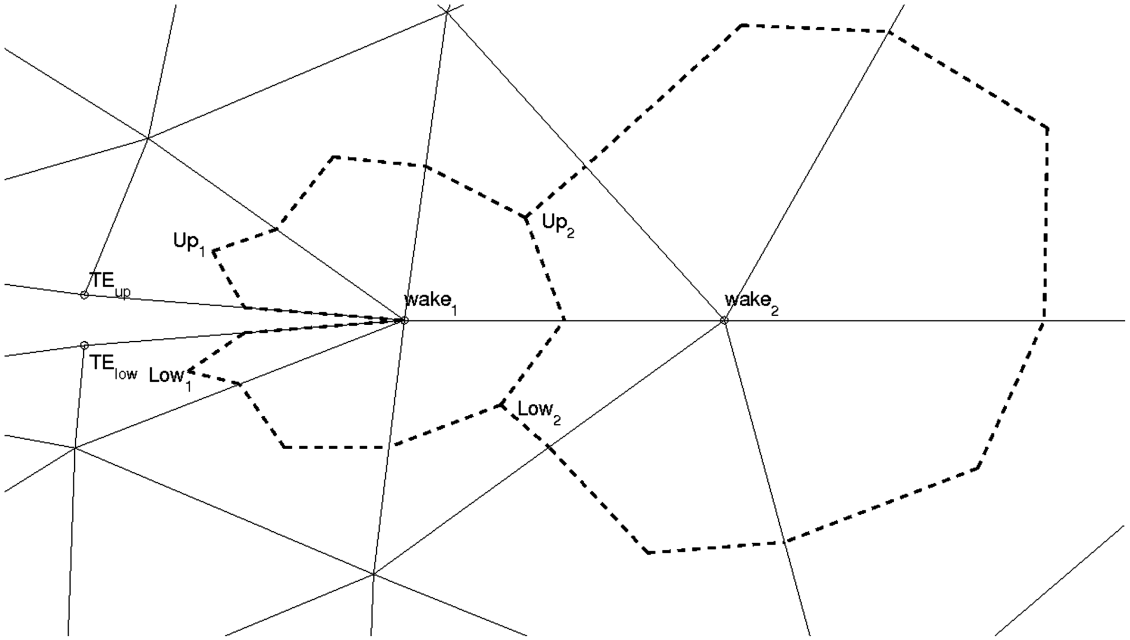


**Fig. 3 Trailing edge mesh detail.**

The discrete form of the wake equation is

$$\left\{\frac{\partial\varphi}{\partial t}\right\}_{\text{up}} - \left\{\frac{\partial\varphi}{\partial t}\right\}_{\text{low}} = -\frac{1}{2}(\{|\nabla\varphi|^2\}_{\text{up}} - \{|\nabla\varphi|^2\}_{\text{low}}) \tag{41}$$

Equations (39–41) constitute a set of nonlinear ordinary differential equations in semiexplicit form. Time marching solutions can be obtained either with explicit or first/second-order implicit integration schemes. Only implicit solutions are considered in this work. See [26] for details about explicit schemes.

### I. Implicit Scheme

Implicit schemes can use far larger time steps than their explicit counterparts. This allows us to obtain a good solution efficiency, without multigrid schemes, provided a suitable Jacobian matrix approximation is available. The simpler backward Euler method is used for steady solutions, while a more accurate second-order scheme is used for unsteady solutions. The second-order accurate implicit method is a two-step implicit scheme with controlled dissipation [27]. It can be written as

$$x^{n+1} = a_0 x^n + a_{-1}x^{n-1} + \Delta t(b_1\dot{x}^{n+1} + b_0\dot{x}^n + b_{-1}\dot{x}^{n-1}) \tag{42}$$

with

$$a_0 = 1-\beta, \quad a_{-1} = \beta, \quad b_1 = \frac{1}{2}+\delta, \quad b_0 = \frac{1+\beta}{2}-2\delta, \quad b_{-1} = \frac{\beta}{2}+\delta$$

The parameters $\beta$ and $\delta$ can be expressed as functions of the desired asymptotic spectral radius $\rho_\infty$:

$$\beta = \frac{4|\rho_\infty|^2 - (1-|\rho_\infty|)^2}{4-(1-|\rho_\infty|)^2}, \qquad \delta = \frac{1-|\rho_\infty|^2}{8-2(1-|\rho_\infty|)^2}$$

The linear stability properties of the scheme can be tuned using the parameter $|\rho_\infty|$. For $|\rho_\infty| = 0$ the method results in the L-stable two-step backward difference formula. For $|\rho_\infty| = 1$, an A-stable two-step form of Crank–Nicolson rule results.

A generic $p$-step implicit scheme can be expressed as

$$\dot{x}^{n+1} = a(\Delta t)x^{n+1} + r(x^n, \ldots, x^{n-(p-1)}, \Delta t) \tag{43}$$

where $a$ is a coefficient and $r$ is a residual term related to the solution at the previous step. The implicit backward Euler scheme gives

$$a = \frac{1}{\Delta t}, \qquad r = -\frac{1}{\Delta t}x^n$$

while the proposed second-order method, Eq. (42), results in

$$a = \frac{1}{b_1\Delta t}$$

$$r = -\frac{1}{b_1\Delta t}(a_0 x^n + a_{-1}x^{n-1}) - \frac{1}{b_1}(b_0\dot{x}^n + b_{-1}\dot{x}^{n-1})$$

Using Eq. (43) in Eqs. (39–41) at step $n+1$ yields

$$[I_\rho](a\{\rho\}^{n+1} + \{r_\rho\}^n) = \{F(\{\rho\}^{n+1}, \{\varphi\}^{n+1})\}^{n+1} \tag{44}$$

$$[I_\varphi](a\{\varphi\}^{n+1} + \{r_\varphi\}^n) = \{E(\{\rho\}^{n+1}, \{\varphi\}^{n+1})\}^{n+1} \tag{45}$$

$$[I_s](a\{\varphi\}^{n+1} + \{r_\varphi\}^n) = \{S(\{\varphi\}^{n+1})\}^{n+1} \tag{46}$$

with

$$\{E\}^{n+1} = \frac{1}{2}\{A\} - \frac{1}{2}[\Sigma]\{|\nabla\varphi|^2\}^{n+1} - \frac{M_\infty^{-2}}{\gamma-1}[I_\rho](\{\rho^{\gamma-1}\}^{n+1} - \{1\}) \tag{47}$$

$$\{S\}^{n+1} = -\frac{1}{2}(\{|\nabla\varphi|^2\}_{\text{up}}^{n+1} - \{|\nabla\varphi|^2\}_{\text{low}}^{n+1}) \tag{48}$$

$[I_s]$ is a Boolean incidence matrix that computes the jump of $\varphi$ at the wake.

Equations (44–46) yield a nonlinear system of equations: $\mathbf{f}(\mathbf{x}^{n+1}) = 0$, which can be solved with Newton–Raphson method:

$$\mathbf{f}(\mathbf{x}_k^{n+1}) + \left(\frac{\partial\mathbf{f}}{\partial\mathbf{x}}\right)_{\mathbf{x}=\mathbf{x}_k^{n+1}}(\mathbf{x}_{k+1}^{n+1} - \mathbf{x}_k^{n+1}) = 0 \tag{49}$$

where $\mathbf{x}_k^{n+1}$ is the solution at the previous iteration and $\frac{\partial\mathbf{f}}{\partial\mathbf{x}}$ is the Jacobian matrix of the problem. To advance the solution, an initial prediction at time step $n+1$ is needed. Either the solution at the previous step or a suitable extrapolation can be used. The latter option is followed in this work, using a cubic interpolation of the solution at two previous steps:

$$\dot{x}^{n+1} = -\frac{12}{\Delta t}x^n + \frac{12}{\Delta t}x^{n-1} + 8\dot{x}^n + 5\dot{x}^{n-1} \tag{50}$$

The terms at the right-hand side of Eqs. (44–46) need to be linearized. The generic flux term in the mass conservation equation, Eq. (44), yields

$$\begin{aligned} F^{n+1} &= \oint_\Sigma \rho^{n+1}\nabla\varphi^{n+1}\cdot n\,\mathrm{d}\Sigma \\ &= \oint_\Sigma (\rho^{n+1} + \Delta\rho^{n+1})\nabla(\varphi^{n+1} + \Delta\varphi^{n+1})\cdot n\,\mathrm{d}\Sigma \end{aligned} \tag{51}$$

Neglecting the second-order term, the flux at step $n+1$ is

$$F^{n+1} = \oint_\Sigma \rho^{n+1}\nabla\varphi^{n+1}\cdot n\,\mathrm{d}\Sigma \tag{52}$$

An increment flux in $\rho$ is

$$\Delta F_\rho^{n+1} = \oint_\Sigma \Delta\rho^{n+1}\nabla\varphi^{n+1}\cdot n\,\mathrm{d}\Sigma \tag{53}$$

while an increment flux in $\varphi$ is

$$\Delta F_\varphi^{n+1} = \oint_\Sigma \rho^{n+1}\nabla(\Delta\varphi^{n+1})\cdot n\,\mathrm{d}\Sigma \tag{54}$$

The vector of the fluxes can be expressed as

$$\{F\}^{n+1} = \{F\}^{n+1} + [F_\rho]^{n+1}\{\Delta\rho\}^{n+1} + [F_\varphi]^{n+1}\{\Delta\varphi\}^{n+1} \tag{55}$$

The Jacobian matrices $[F_\rho]$ and $[F_\varphi]$ can be calculated by writing the flux expression in a different way. The Jacobian matrix related to $\rho$ is obtained by writing the flux as a product by $\rho$. After defining the matrices

$$[f_i] = \sum_k (\mathrm{diag}\{\hat{n}_k^i\}[G_{\varphi k}]) \tag{56}$$

the fluxes vector becomes

$$\{F\} = \sum_i ([B_i]\mathrm{diag}([f_i]\{\varphi\}))([B_g] + [U])\{\rho\} = [F_\rho]\{\rho\} \tag{57}$$

The same vector can be expressed as a product by $\varphi$:

$$\{F\} = \sum_i ([B_i]\mathrm{diag}(([B_g] + [U])\{\rho\})[f_i])\{\varphi\} = [F_\varphi]\{\varphi\} \tag{58}$$

The generic Laplacian term of $\varphi$ in the Bernoulli equation, Eq. (47), becomes

$$(\nabla\varphi^{n+1})^2 = \nabla(\varphi^{n+1} + \Delta\varphi^{n+1})\cdot\nabla(\varphi^{n+1} + \Delta\varphi^{n+1}) \tag{59}$$

Neglecting the second-order term, we obtain

$$(\nabla\varphi^{n+1})^2 = \nabla\varphi^{n+1}\cdot\nabla\varphi^{n+1} + 2\nabla\varphi^{n+1}\cdot\nabla(\Delta\varphi^{n+1}) \tag{60}$$

Then the second term in Eq. (47) can be approximated as

$$-[\Sigma]\frac{\{|\nabla\varphi|^2\}}{2} = -[\Sigma]\frac{\{|\nabla\varphi|^2\}}{2} + [E_\varphi]\{\Delta\varphi\} \tag{61}$$

where the Jacobian matrix is

$$[E_\varphi] = -[\Sigma]\sum_k (\mathrm{diag}([G_{\varphi k}]\{\varphi\})[G_{\varphi k}]) \tag{62}$$

The last term in Eq. (47) becomes

$$\begin{aligned} &-\frac{M_\infty^{-2}[I_\rho]}{\gamma-1}(\{\rho^{\gamma-1}\}^{n+1} - \{1\}) \\ &\quad = -\frac{M_\infty^{-2}[I_\rho]}{\gamma-1}(\{\rho^{\gamma-1}\}^{n+1} - \{1\}) + [E_\rho]^{n+1}\{\Delta\rho\}^{n+1} \end{aligned} \tag{63}$$

where the Jacobian matrix is

$$[E_\rho] = -M_\infty^{-2}\mathrm{diag}\{\rho^{\gamma-2}\}[I_\rho] \tag{64}$$

The second member of Eq. (48), with Eq. (60), becomes

$$\begin{aligned} &\{|\nabla\phi|^2\}_{\mathrm{up}}^{n+1} - \{|\nabla\phi|^2\}_{\mathrm{low}}^{n+1} \\ &\quad = \{|\nabla\phi|^2\}_{\mathrm{up}}^{n+1} - \{|\nabla\phi|^2\}_{\mathrm{low}}^{n+1} - 2[S_\varphi]^{n+1}\{\Delta\phi\}^{n+1} \end{aligned} \tag{65}$$

where the Jacobian matrix is

$$\begin{aligned} [S_\varphi] &= -\sum_k (\mathrm{diag}([G_{\varphi k}]_{\mathrm{up}}\{\varphi\})[G_{\varphi k}]_{\mathrm{up}}) \\ &\quad + \sum_k (\mathrm{diag}([G_{\varphi k}]_{\mathrm{low}}\{\varphi\})[G_{\varphi k}]_{\mathrm{low}}) \end{aligned} \tag{66}$$

$[G_{\varphi k}]_{\mathrm{up}}$ and $[G_{\varphi k}]_{\mathrm{low}}$ are submatrices of the gradient operator $[G_{\varphi k}]$, built with the rows related to the elements up and low of the wake.

The global solution, residual and function vectors are defined as

$$\{x\} = \begin{Bmatrix}\{\rho\}\\ \{\varphi\}\end{Bmatrix}, \qquad \{r_x\} = \begin{Bmatrix}\{r_\rho\}\\ \{r_\varphi\}\end{Bmatrix}, \qquad \{f\} = \begin{Bmatrix}\{F\}\\ \{E\}\\ \{S\}\end{Bmatrix}$$

The global integration and Jacobian matrices are

$$[I_x] = \begin{bmatrix}[I_\rho] & [0]\\ [0] & [I_\varphi]\\ [0] & [I_s]\end{bmatrix}, \qquad [J_x] = \begin{bmatrix}[F_\rho] & [F_\varphi]\\ [E_\rho] & [E_\varphi]\\ [0] & [S_\varphi]\end{bmatrix}$$

The solution $\{x\}$ and the function $\{f\}$ at iteration $k+1$ of step $n+1$ are

$$\{x\}_{k+1}^{n+1} = \{x\}_k^{n+1} + \{\Delta x\}_{k+1}^{n+1} \tag{67}$$

$$\{f\}_{k+1}^{n+1} = \{f\}_k^{n+1} + [J_x]_k^{n+1}\{\Delta x\}_{k+1}^{n+1} \tag{68}$$

The application of the integration scheme, Eq. (43), yields

$$(a[I_x] - [J_x]_k^{n+1})\{\Delta x\}_{k+1}^{n+1} = \{f\}_k^{n+1} - \{r_x\}^n - a[I_x]\{x\}_k^{n+1} \tag{69}$$

Solving Eq. (69) we obtain the solution vector for the $(k+1)$th iteration. We iterate a fixed number of times or until

$$\left\| \left\{\frac{\Delta\rho}{\rho}\right\}_{k+1}^{n+1} \right\|_\infty > \mathrm{tol} \tag{70}$$

It can be seen that the number of per time step operations required by the implicit scheme far exceeds that of an explicit scheme. Nonetheless it surpasses a trivial implementation of its explicit counterpart because of the possibility of using far larger time steps. It is here speculated that it can remain competitive even against a multigrids-based explicit implementation, because the Jacobian calculation illustrated above is simpler than multi grids iterations on unstructured meshes. Such a speculation should deserve a verification nonetheless. Moreover the implicit formulation of the present paper can be trivially passed to available efficient free(dom) general purpose sparse matrix operations packages and solvers for nonlinear systems of equations based on state of the art matrix free, scalar and parallel, gradient-based implementations that can provide far more efficiency than those reported in the following test applications. In fact due to the somewhat proof of concept nature of the present paper, we will simply couple the CSparse [28] matrix package to the general purpose exact sparse multifrontal LU solution routine available in UMFPACK [29–32], to solve the global system, Eq. (69), and use Newton–Raphson iterations.

Within such a scheme the unchanging sparse layout of the Jacobian matrix has been exploited by carrying out the, somewhat costly, numerically balanced fill in optimization only once, reusing it unchanged in all of the following iterated solutions. Despite the use of such a somewhat trivial optimization, a standard tool of the sparse solver used, the promising calculation times that will be shown should adequately depict the validity of the two-fields approach with

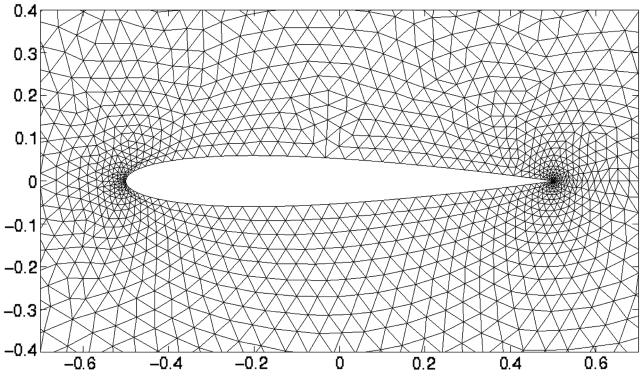


**Fig. 4 Coarse grid (airfoil detail).**

respect to both simplicity and efficiency of the related numerical implementation.

### J. Stability Analysis

A nonlinear multidimensional stability analysis poses considerable problems. A standard one-dimensional stability evaluation on the linearized formulation of the problem

$$\frac{\partial \rho}{\partial t} + \frac{\partial}{\partial x}\left(\rho \frac{\partial \varphi}{\partial x}\right) = 0 \tag{71}$$

$$\frac{\partial \varphi}{\partial t} + \frac{1}{2}\left(\left(\frac{\partial \varphi}{\partial x}\right)^2 - 1\right) + \frac{M_\infty^{-2}}{\gamma - 1}(\rho^{\gamma-1} - 1) = 0 \tag{72}$$

is considered instead. After defining the incremented functions, $\rho = \rho_\infty + \rho$ and $\varphi = \varphi_\infty + \varphi$, where $\rho_\infty = V_\infty = 1$, the linearized formulation can be written:

$$\frac{\partial \rho}{\partial t} + \frac{\partial \rho}{\partial x} + \frac{\partial^2 \varphi}{\partial x^2} = 0 \tag{73}$$

$$\frac{\partial \varphi}{\partial t} + \frac{\partial \varphi}{\partial x} + M_\infty^{-2}\rho = 0 \tag{74}$$

A one-dimensional finite volume solution of Eqs. (73) and (74) is $h$ equivalent to a centered finite difference scheme using

$$u'_j = \frac{u_{j+1} - u_{j-1}}{2h} + \mathcal{O}(h^2) \tag{75}$$

$$u''_j = \frac{u_{j+1} - 2u_j + u_{j-1}}{h^2} + \mathcal{O}(h^2) \tag{76}$$

A further simplification can be obtained by assuming a single time step unsteady solver, i.e., using the following implicit finite difference in time:

$$\dot{u}^{\,n+1} = \frac{u^{n+1} - u^n}{\Delta t} + \mathcal{O}(\Delta t) \tag{77}$$

A Von Neumann analysis [25] applied to any resulting difference scheme in the form

$$u_j^n = \sum_{k=-\infty}^{\infty} \alpha_k e^{ikih} \gamma_k^n \tag{78}$$

where $\gamma_k \in C$ is the amplification coefficient related to the frequency $k$, proves that a scheme is strongly stable if $|\gamma_k| \leq 1 \ \forall \ k$ can be demonstrated [25].

A backward centered Euler scheme is considered for simplicity, see [26] for a more comprehensive analysis. Equations (75–77), after using Eqs. (73) and (74), allow to write

$$\rho_j^{n+1} = \rho_j^n - \frac{\Delta t}{h}\frac{\rho_{j+1}^{n+1} - \rho_{j-1}^{n+1}}{2} - \frac{\Delta t}{h^2}(\varphi_{j+1}^{n+1} - 2\varphi_j^{n+1} + \varphi_{j-1}^{n+1}) \tag{79}$$

$$\varphi_j^{n+1} = \varphi_j^n - \frac{\Delta t}{h}\frac{\varphi_{j+1}^{n+1} - \varphi_{j-1}^{n+1}}{2} - M_\infty^{-2}\Delta t \rho_j^{n+1} \tag{80}$$

Considering: $u_{j+1} = u_j e^{ikh}$, $u_{j-1} = u_j e^{-ikh}$, $e^{ix} - e^{-ix} = 2i\sin(x)$, $e^{ix} + e^{-ix} = 2\cos(x)$, we obtain

$$\begin{Bmatrix} \rho \\ \varphi \end{Bmatrix}_j^n = \begin{bmatrix} 1 + i\Delta t/h \sin(kh) & 2\Delta t/h^2(\cos(kh) - 1) \\ M_\infty^{-2}\Delta t & 1 + i\Delta t/h \sin(kh) \end{bmatrix} \begin{Bmatrix} \rho \\ \varphi \end{Bmatrix}_j^{n+1} \tag{81}$$

The eigenvalues of the matrix in Eq. (81) can be expressed as function of the Courant, Friedrichs, and Lewy number (CFL), where $\mathrm{CFL} = M_\infty^{-1}\Delta t/h$:

$$\gamma_{1,2} = 1 + i\mathrm{CFL}(M_\infty \sin(kh) \pm \sqrt{2 - 2\cos(kh)}) \tag{82}$$

The implicit scheme is strongly stable for any values of $k$, $M_\infty$ and CFL.

## IV. Numerical Results

Some results obtained with the developed code, named TFFP (two-fields full potential), are discussed to validate the proposed approach.

Because of the lack of a viable interface to three-dimensional mesh generators, two-dimensional results will be discussed more extensively. In fact, three-dimensional results are used to provide a proof of the general validity of the two-fields approach, by verifying two-dimensional results obtained for a three-dimensional wing confined by walls parallel to the asymptotic flow.

### A. Two-Dimensional Steady Analyses

A NACA 0012 airfoil modeled within a circular mesh with a radius equal to four chords is considered for two-dimensional analyses. A mesh having 4376 elements and 2252 nodes is termed coarse grid (see Fig. 4), while a mesh with 17,504 elements and 8881 nodes obtained by dividing each triangle of the coarse grid into four triangles is termed fine grid.

Figure 5 compares the results for lifting configurations achieved through an exact rotation of the asymptotic flow with the corresponding transpiration on the body surface, for subcritical and supercritical condition.

The transpiration technique allows us to easily obtain good results for small perturbations in unsteady conditions.

Figure 6 compares two subcritical configurations with the results presented in [33].

For a stronger supercritical configuration, Fig. 7 compares the results of FLO36 [34], MSES [35] with those of two TFFP options. The TFFP option referred as modified applies the shock condition discussed in Sec. III.G. This technique allows us to accurately capture a shock, even within a somewhat coarse grid, but does not constitute an entropy correction for the solution.

In fact when the shock location and strength from potential transonic solutions are compared with solutions from the Euler equations a general trend can be observed. Because of the isentropic assumption, the potential shock strength is always stronger than a shock from an Euler solution. This in turn causes the location of the shock to be further downstream on an airfoil or wing. Such an effect is stronger the higher the Mach number is.

### B. Two-Dimensional Unsteady Analyses

A thin plate subject to step angle of attack is considered.

Figure 8 compares TFFP results with those of the linear theory related to a thin plate [36], highlighting the initial transient phase against piston theory [36].

With the same thin plate, the proposed approach can be compared with incompressible Theodorsen's theory [37] for a plunging-pitching two-dimensional plane plate. Theodorsen's harmonic solution provides a benchmark for any newly developed computational fluid dynamics scheme.

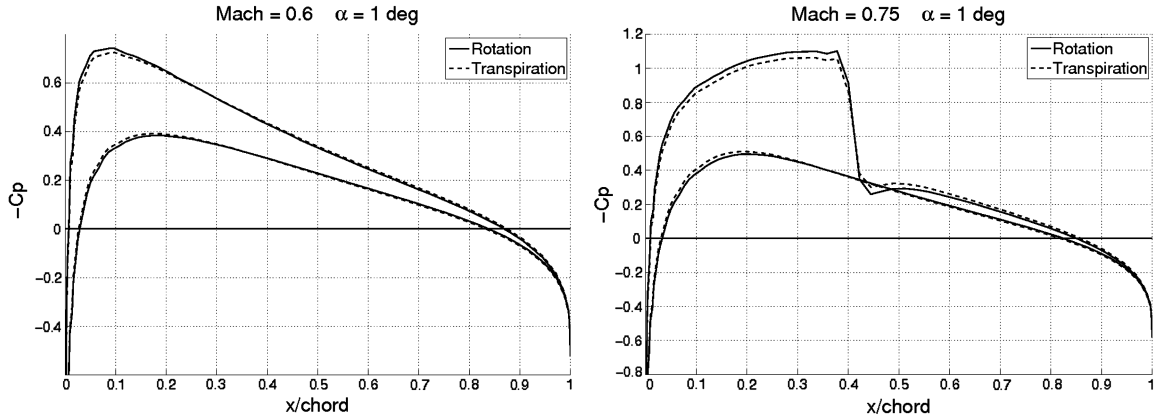


**Fig. 5 Pressure distribution over NACA 0012 obtained with rotation and transpiration (fine grid).**

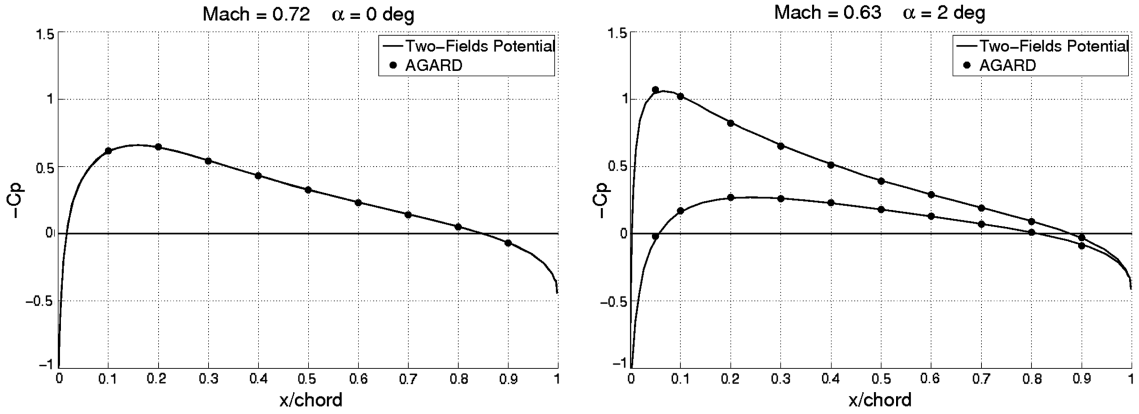


**Fig. 6 Pressure distribution over NACA 0012 for the code and AGARD results (coarse grid).**

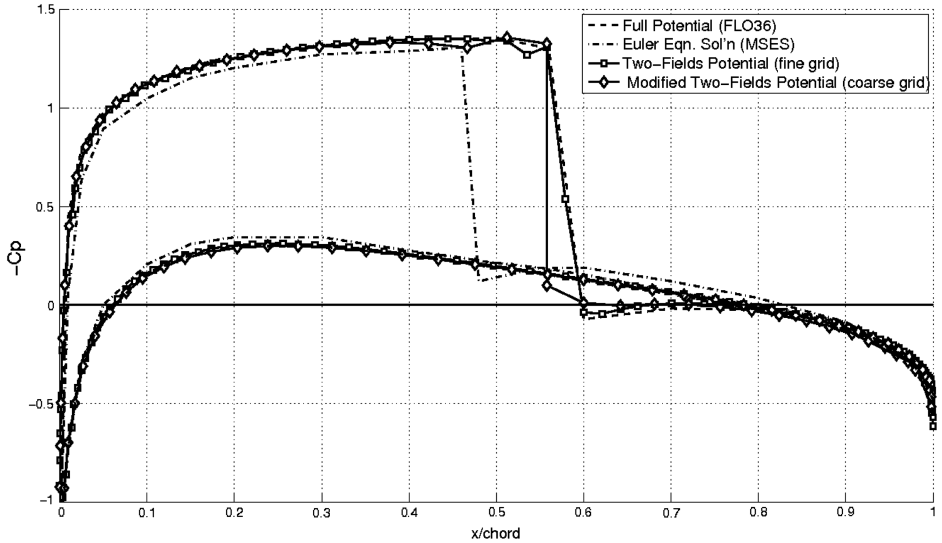


**Fig. 7 Pressure distribution over NACA 0012: $M = 0.75$, $\alpha = 2$ deg.**

The plunge motion $h$ and the pitch motion $\theta$ are related to the lift coefficient $C_L$ and the moment coefficient $C_M$ (referred to the quarter chord location) in the frequency domain with the reduced frequency $k$ through the aerodynamic transfer functions matrix $H_{\text{am}}$:

$$\begin{Bmatrix} C_L(k) \\ C_M(k) \end{Bmatrix} = [H_{\text{am}}(k)] \begin{Bmatrix} h(k) \\ \theta(k) \end{Bmatrix} \tag{83}$$

The incompressible condition is approximated with $M_\infty = 0.01$. Figure 9 shows a good agreement with Theodorsen's theory.

The above results indicate that the two-fields approximation does not lose accuracy at very low Mach numbers. Moreover, the efficient linearization provided by transpiration boundary conditions, coupled to a procedure that allows the determination of aerodynamic transfer matrices through appropriately imposed transient motion [38], allows the use of the proposed approach in transonic flutter analyses

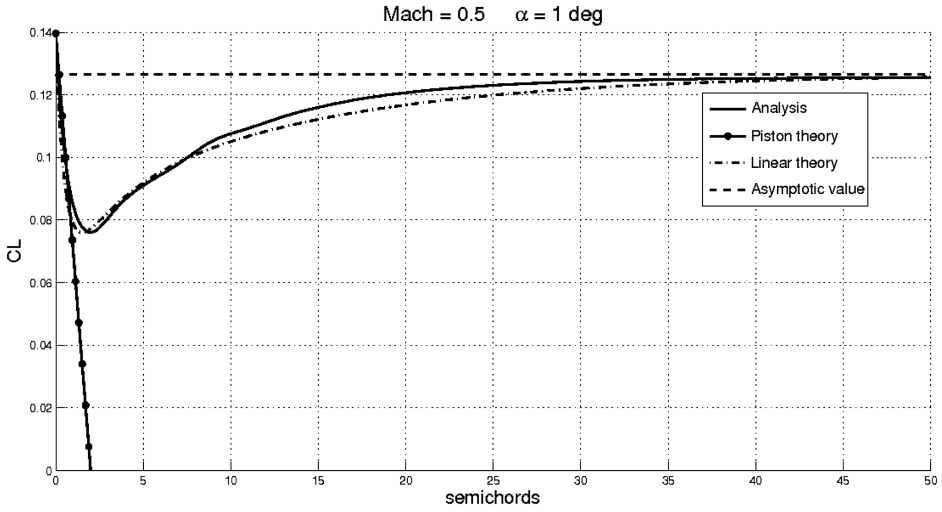


**Fig. 8 Response of thin plate to step angle of attack.**

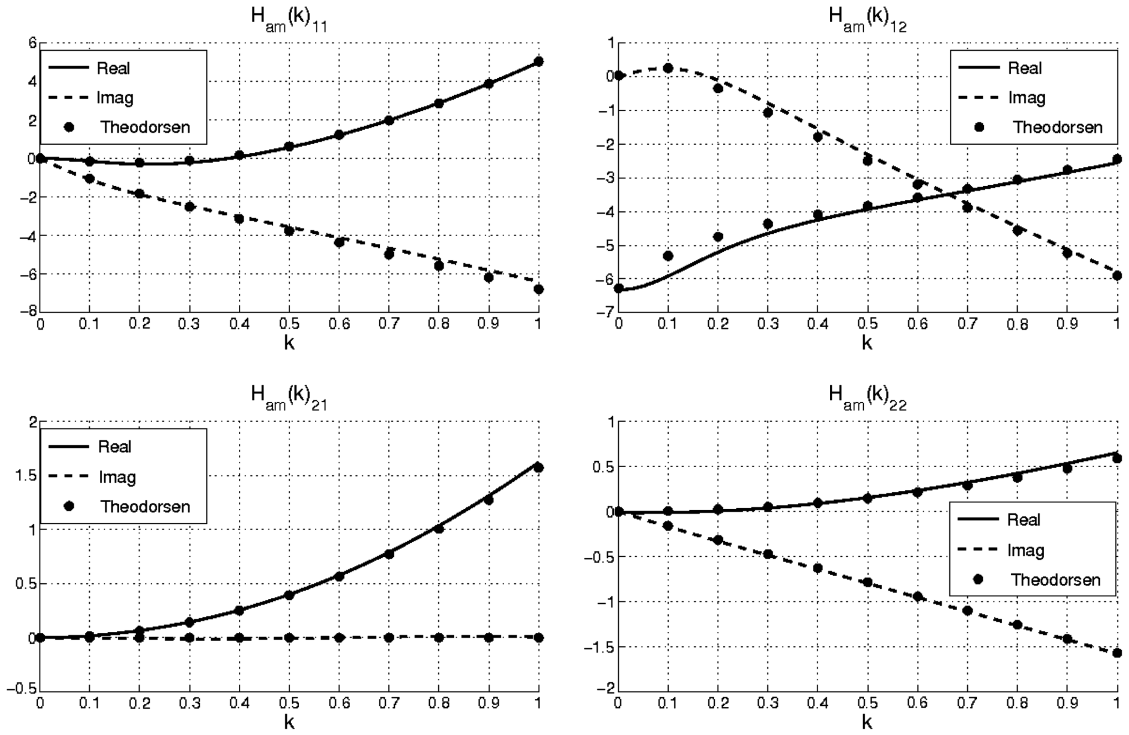


**Fig. 9 Aerodynamic transfer functions matrix $H_{\mathrm{am}}$ at $M = 0.01$.**

based on the strip theory, still used profitably for high aspect ratio wings, in conceptual-preliminary designs especially.

A final unsteady two-dimensional analysis concerns the response of the NACA 0012 airfoil subjected to an harmonic pitching oscillation around the quarter chord location. The number of cycles required for a steady response grows with the frequency.

In Fig. 10, the marker points identify the limit cycles obtained with the PICO2D [24] code, which solves the FP equations with a structured finite volume scheme in a moving grid.

### C. Three-Dimensional Analyses

For a three-dimensional test, a rectangular NACA0012 constant section wing bounded by a wall parallel to the asymptotic flow at both of its ends is used. The related three-dimensional mesh is obtained by extruding the two-dimensional fine grid previously described for a total of five span sections, so totaling 44,405 nodes and 210,048 elements. This allows us to verify the three-dimensional results of the two-fields approach by checking the matching with the corresponding two-dimensional results at any station. Figure 11 presents two sample verifications for the steady case and for the response of the wing to a step variation of angle of attack.

The figure confirms a perfect matching. This allows us to reasonably assume that no major problem will arise using the two-fields approach for more realistic configurations, as soon as a suitable interface with an efficient three-dimensional meshing support is available.

### D. Computational Performance

As an indication of the computational efficiency achievable with a two-fields approach, typical execution parameters and times are reported. The analyses have been performed on a 2.33 Ghz CPU and a 4 GB 800 Mhz RAM. Table 1 lists steady analyses discussed in Sec. IV.A. For each analysis the number of inner Newton iterations and the CFLs that provide the best convergence are reported, along with the number of time steps required to achieve a steady state lift

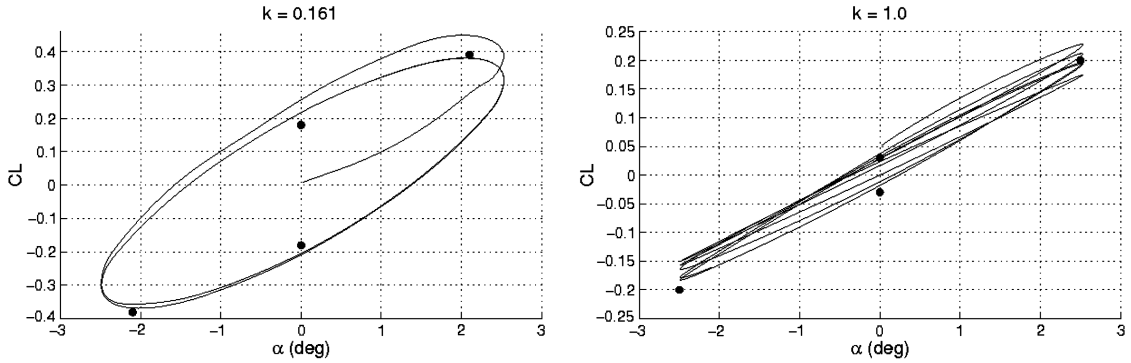


**Fig. 10 Lift coefficient versus angle of attack: $\alpha(t) = .02 + 2.51\sin(kt)$, $M = 0.755$.**

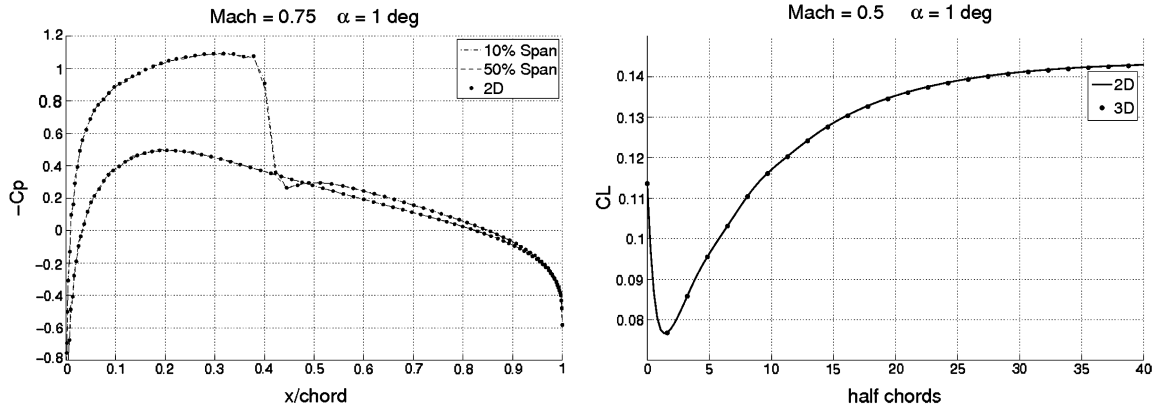


**Fig. 11 Pressure distribution over rectangular wing (left) and response to step angle of attack (right).**

within a relative error of $10^{-4}$. These results allow to infer also a per time step execution time achievable in transient response analyses.

Although only a somewhat simple and proof of concept implementation is available, the authors believe that the two-fields approximation shows good efficiency along with substantial unconditional stability for significantly nonlinear calculations, namely with CFLs in excess of $10^5$.

The three-dimensional result shown in Fig. 11 on the left has been achieved in four time steps for a total CPU time of 200 s. Considering that the use of an exact linear solver is not the best choice for large three-dimensional calculations, similar conclusions can be inferred from data related to a sample three-dimensional calculation reported above. The very small number of iterations required to achieve steady state by just throwing the wing into the unperturbed flow should be a good enough support for this claim.

## V. Conclusions

The proposed two-fields formulation considerably simplifies the development of the numerical approximation of unsteady FP flows, leading to a simple, precise and robust resolution scheme.

The results obtainable with such a scheme are not affected even by adopting a simplified, somewhat more efficient, numerical implementation for the calculation of internal fluxes, based on a constant density evaluated at the center of each element.

The improved density upwinding developed in the present work, by taking into account the geometry of the Mach cones at the element vortices, avoids any numerical tuning and yields a continuous upwind activation, greatly contributing to the numerical stability of the method.

Moreover the two-fields scheme allows us to sharply capture embedded shocks, even within relatively coarse meshes, by making it simple introducing a density change across the shock while keeping the potential continuous.

The node-based unstructured finite volume discretization scheme adopted leads to a set of nonlinear ordinary differential equations whose time marching solutions can be obtained through first/second-order implicit integration schemes, whose unconditional linearized stability properties have been demonstrated.

Numerical results well match analytical and alternative numerical solutions. The related calculation times should adequately depict the validity of the two-fields approach with respect to both simplicity and efficiency of the related unstructured numerical implementation. It should be noted also that a possible nonlinear unconditional stability can be inferred by the possibility of using very high CFL numbers for inaccurate transients responses leading to steady solutions.

**Table 1 Two-dimensional steady analyses for NACA0012**

| Figure | $M_\infty$ | $\alpha$, deg | $CFL_{max}$ | Nodes | Time steps | Newton iteration | CPU time, s |
|---|---|---|---|---|---|---|---|
| 6 left | 0.72 | 0 | $10^6$ | 2252 | 1 | 3 | 0.29 |
| 6 right | 0.63 | 2 | $10^6$ | 2252 | 2 | 3 | 0.36 |
| 7 coarse | 0.75 | 2 | $10^6$ | 2252 | 5 | 3 | 0.95 |
| 5 left | 0.60 | 1 | $10^6$ | 8881 | 3 | 3 | 2.13 |
| 5 right | 0.75 | 1 | $10^6$ | 8881 | 4 | 3 | 4.93 |
| 7 fine | 0.75 | 2 | $2 \cdot 10^5$ | 8881 | 15 | 2 | 12.48 |

## References


[1] Murman, E. M., and Cole, J. D., "Calculation of Plane Steady Transonic Flows," *AIAA Journal*, Vol. 9, No. 1, 1971, pp. 114–121. doi:10.2514/3.6131

[2] Steger, J. L., and Lomax, H., "Transonic Flow About Two-Dimensional Airfoils by Relaxation Procedures," *AIAA Journal*, Vol. 10, No. 1, 1972, pp. 49–54. doi:10.2514/3.50066

[3] Garabedian, P. R., and Korn, D., "Analysis of Transonic Airfoils," *Communications on Pure and Applied Mathematics*, Vol. 24, No. 6, 1971, pp. 841–851. doi:10.1002/cpa.3160240608

[4] Ballhaus, W. F., and Bailey, F. R., "Numerical Calculation of Transonic Flow About Swept Wings," AIAA Fifth Fluid and Plasma Dynamics Conference, Boston, MA, 26–28 June 1972.

[5] Bailey, F. R., and Steger, J. L., "Relaxation Techniques for Three-Dimensional Transonic Flow About Wings," AIAA 10th Aerospace Sciences Meeting, San Diego, CA, 17–19 Jan. 1972.

[6] Jameson, A., "Iterative Solutions of Transonic Flows Over Airfoils and Wings, Including Flows at Mach 1," *Communications on Pure and Applied Mathematics*, Vol. 27, No. 3, 1974, pp. 283–309. doi:10.1002/cpa.3160270302

[7] Murman, E. M., "Analysis of Embedded Shock Waves Calculated by Relaxation Methods," *AIAA Journal*, Vol. 12, No. 5, 1974, pp. 626–635. doi:10.2514/3.49309

[8] Jameson, A., "Transonic Potential Flow Calculations Using Conservative Form," AIAA Second Computational Fluid Dynamics Conference, Hartford, CT, 1975.

[9] Glowinsky, R., Periaux, J., and Pironneau, O., "Transonic Flow Simulation by the Finite Element Method via Optimal Control," *Finite Elements in Fluids*, Vol. 3, 1978, pp. 205–217.

[10] Ecer, A., and Akay, H. U., "Application of Finite Element Method for the Solution of Transonic Flow," *Finite Elements in Fluids*, Vol. 3, June 1976, pp. 191–201.

[11] Jameson, A., and Caughey, D. A., "Transonic Potential Flow Calculations Using Conservative Form," Proceedings of the AIAA Third Computational Fluid Dynamics Conference, Albuquerque, NM, 1977.

[12] Hafez, M. M., South, J. C., and Murman, E. M., "Artificial Compressibility Methods for the Numerical Solution of the Full Potential Equation," *AIAA Journal*, Vol. 17, No. 8, 1979, pp. 838–844. doi:10.2514/3.61235

[13] Jameson, A., "Acceleration of Transonic Potential Flow Calculations on Arbitrary Meshes by the Multi-Grid Method," AIAA Paper 79-1458, July 1979.

[14] Boerstoel, J. W., "A Multi-Grid Algorithm for Steady Transonic Potential Flows Around Airfoils Using Newton Iteration," *Journal of Computational Physics*, Vol. 48, No. 3, 1982, pp. 314–343.

[15] Van der Wees, A. J., Van der Vooren, J., and Meelker, J. H., "Robust Calculation of 3D Transonic Potential Flow Based on the Non-Linear FAS Multi-Grid Method and Incomplete LU Decomposition," AIAA Paper 83-1950, 1983.

[16] Engquist, B., and Osher, S., "Stable and Entropy Satisfying Approximations for Transonic Flow Calculations," *Mathematics of Computation*, Vol. 34, No. 149, 1980, pp. 45–75. doi:10.2307/2006220

[17] Osher, S., "Shock Modelling in Aeronautics," *Numerical Methods for Fluid Dynamics*, Academic Press, London, 1982, pp. 179–218.

[18] Volpe, G., and Jameson, A., "Transonic Potential Flow Calculations by Two Artificial Density Methods," *AIAA Journal*, Vol. 26, No. 4, 1988, pp. 425–429.

[19] Holst, T. L., "Numerical Solution of the Full Potential Equation Using a Chimera Grid Approach," NASA TM-110360, 1995.

[20] Neel, R. E., "Advances in Computational Fluid Dynamics: Turbulent Separated Flows and Transonic Potential Flows," Ph.D. Thesis, Virginia Polytechnic Inst. and State Univ., Blacksburg, VA, 1997.

[21] Hirsch, C., "*Numerical Computation of Internal and Esternal Flows*," Wiley, New York, 1988.

[22] Morino, L., and Gennaretti, M., "Boundary Integral Equation Methods for Aerodynamics," *Computational Nonlinear Mechanics in Aerospace Engineering*, edited by S. N. Atluri, Progress in Aeronautics and Astronautics, Vol. 146, AIAA, Washington, D.C., 1992, pp. 279–321.

[23] Shankar, V., Ide, H., and Osher, S., "A Fast Time-Accurate Unsteady Full Potential Scheme," AIAA Seventh Computational Fluid Dynamics Conference, Cincinnati, OH, 1985.

[24] Gasparini, L., "Soluzione a Potenziale di Correnti Transoniche Non Stazionarie su Pale Rotanti," Ph.D. Thesis, Politecnico di Milano, Italy, 1995.

[25] Quarteroni, A., *Modellistica Numerica per Problemi Differenziali*, Springer, New York, 2006.

[26] Parrinello, A., "Soluzione a due campi per Correnti a Potenziale Transoniche Instazionarie," Thesis, Politecnico di Milano, Italy, 2008.

[27] Masarati, P., Lanz, M., and Mantegazza, P., "Multistep Integration of Ordinary, Stiff and Differential-Algebraic Problems for Multibody Dynamics Applications," *16th Congresso Nazionale AIDAA*, Palermo, Italy, Sep. 2001, pp. 1–10.

[28] Davis, T. A., *Direct Methods for Sparse Linear Systems*, SIAM Series on the Fundamentals of Algorithms, SIAM, Philadelphia, 2006.

[29] Davis, T. A., "A Column Pre-Ordering Strategy for the Unsymmetric-Pattern Multifrontal Method," *ACM Transactions on Mathematical Software*, Vol. 30, No. 2, June 2004, pp. 165–195. doi:10.1145/992200.992205

[30] Davis, T. A., "Algorithm 832: UMFPACK, an Unsymmetric-Pattern Multifrontal Method," *ACM Transactions on Mathematical Software*, Vol. 30, No. 2, June 2004, pp. 196–199. doi:10.1145/992200.992206

[31] Davis, T. A., and Duff, I. S., "A Combined Unifrontal/Multifrontal Method for Unsymmetric Sparse Matrices," *ACM Transactions on Mathematical Software*, Vol. 25, No. 1, March 1999, pp. 1–19. doi:10.1145/305658.287640

[32] Davis, T. A., and Duff, I. S., "An Unsymmetric-Pattern Multifrontal Method for Sparse LU Factorization," *SIAM Journal on Matrix Analysis and Applications*, Vol. 18, No. 1, Jan. 1997, pp. 140–158. doi:10.1137/S0895479894246905

[33] Lock, R. C., "Test cases for Numerical Methods in Two-Dimensional Transonic Flows," AGARD Rept. No. 575, 1970.

[34] Jameson, A., "Acceleration of Transonic Potential Flow Calculations on Arbitrary Meshes by the Multi-Grid Method," AIAA Paper 79-1458, 1979.

[35] Mason, W. H., "Some Transonic Aerodynamics," www.aoe.vt.edu.

[36] Bisplinghoff, R. L., Ashely, H., and Halfman, R. L., *Aeroelasticity*, Dover, New York, 1996.

[37] Theodorson, T., "General Theory of Aerodynamic Instability and the Mechanism of Flutter," NACA, TR-496, 1935.

[38] Martegani, M., "Un Metodo per il Calcolo del Flutter Linearizzato in Regime Transonico," Politecnico di Milano, Italy, 2003.


E. Livne
*Associate Editor*